CONTROL AND INFORMATICS

Fault detection for DFIG based on sliding mode observer of new reaching law

RuiQi LI[1,3], WenXin YU[1,3]*, JunNian WANG[2,3], Yang LU[1,3], Dan JIANG[1,3], GuoLiang ZHONG[1,3], and ZuanBo ZHOU[1,3]

[1] School of Information and Electrical Engineering, Hunan University of Science and Technology, Hunan Pro., Xiangtan,411201, China
[2] School of Physics and Electronics, Hunan University of Science and Technology, Hunan Pro., Xiangtan,411201, China
[3] Key Laboratory of Knowledge Processing Networked Manufacturing, Hunan University of Science and Technology, Hunan Pro., Xiangtan,411201, China

Abstract. For fault detection of doubly-fed induction generator (DFIG), in this paper, a method of sliding mode observer (SMO) based on a new reaching law (NRL) is proposed. The SMO based on the NRL (NRL- SMO) theoretically eliminates system chatter caused by the reaching law and can be switched in time with system interference in terms of robustness and smoothness. In addition, the sliding mode control law is used as the index of fault detection. Firstly, this paper gives the NRL with the theoretically analyzes. Secondly, according to the mathematical model of DFIG, NRL-SMO is designed, and its analysis of stability and robustness are carried out. Then this paper describes how to choose the optimal parameters of the NRL-SMO. Finally, three common wind turbine system faults are given, which are DFIG inter-turn stator fault, grid voltage drop fault, and rotor current sensor fault. The simulation models of the DFIG under different faults is established. The simulation results prove that the superiority of the method of NRL-SMO in state tracking and the feasibility of fault detection.

Key words: fault detection; doubly-fed induction generator; sliding mode observer; new reaching law.

1. Introduction

Wind power generators have long been working in inaccessible environments such as deserts, Gobi, and the sea. They are often accompanied by severe weather such as blizzards, typhoons, sandstorms, and thunderstorms. When the wind power generation system fails, it is difficult for humans to go to the fault site for timely detection and maintenance. The traditional fault detection technology is challenging to detect the early faults of the system accurately, forcing the wind turbine to be in a state of fault. When the wind turbine is in trouble for a long time, it will shut down the wind turbine and even damage the electrical equipment. Therefore, seeking an online fault detection technology that is sensitive to early faults has important practical significance. At present, there are many kinds of fault detection technologies for wind turbines. In this paper, fault detection and diagnosis technologies based on state estimation are studied mainly for electrical system faults and sensor faults [1].

The winding faults of the rotor and the stator are the leading electrical faults of the generator [2, 3]. Reference [4] introduces a method of detecting stator winding faults based on the measurement signal of a built-in sensor based on a frequency converter, which can be easily detected, even the single-phase short-circuit fault of the stator winding.However, this method is limited to detection during startup and cannot be applied during machine operation. In [5], a new fault diagnostic index is proposed based on normalized energy evaluation of the given signal using the discrete wavelet transform. Analysis of the simulation results confirms that the proposed fault diagnostic index can accurately discriminate between inter-turn short-circuit fault even with minor shorted turns, winding resistive asymmetrical fault, or unbalanced voltages except for the cases with minor asymmetry and healthy conditions of the stator winding. Reference [6] presents a new online diagnostic approach for the detection of stator and rotor inter-turn short circuit faults in DFIG for wind power applications. It can be used effectively for different generator operating conditions, except that rotor faults cannot be detected in the vicinity of the synchronous speed. In [7], the doubly-fed induction generator (DFIG) stator fault in the slot location is studied because of the special topological structure and the real factors of the generator model. It determines the pulsating magnetomotive force (MMF) expressions mapped to the shorted position in two forms. Based on 2D discretization and piecewise interpolation, a modified fault is developed.

In the operation of DFIG connected to the grid, if there is a fault on the grid side, it is easy to be off the grid, which directly affects the safe and reliable operation of the primary grid. For the grid-side faults, reference [8] presents a new control approach for enhancing the fault ride-through capability of wind farms connected to the grid through a voltage-source-converter-based high-voltage dc transmission line. A controlled voltage drop in the wind farm collector grid is initiated upon a fault in the high-voltage grid to achieve fast power reduction. Ref-

R.Q. Li, W.X. Yu, J.N. Wang, Y. Lu, D. Jiang, G.L. Zhong, and Z.B. Zhou

erence [9] proposes a new stability solution based on PLL frequency for the instability of the grid-side converter of the wind turbine. Because DFIG-based wind turbine has the characteristic of transient fault with low voltage ride through (LVRT) capability, in [10], a new three-phase fault direction identification method for the outgoing transmission line of the wind farm is presented. Reference [11] proposes a decoupled fault ride-through strategy for a doubly fed induction generator (DFIG) to enhance network stability during grid disturbances. It can improve both the active and reactive power capability during fault ride-through operation.

For most electrical fault monitoring, it is still carried out based on the measurement of the current. The current sensor is composed of multiple components, which also has the possibility of damage. Once the current sensor fails, it will directly cause the wrong judgment of the motor control system, resulting in control failure and more significant loss [12, 13]. In [14], for a class of nonlinear Itô stochastic systems, a new observer method based on sliding mode control is proposed to accurately estimate system state, sensor faults, and disturbances at the same time. Reference [15] suggests a current and position sensor fault detection and isolation algorithm with parity equation for driving motor of In-wheel independent drive electric vehicle. This fault detection and diagnosis method with the parity equation can be extended to other systems as well. Reference [16] presents a switching fault-tolerant control (SFTC) strategy for a DFIG-based wind turbine subject to rotor and stator current sensor faults. The proposed SFTC strategy is able to provide superb transient and steady-state performance, strong robustness to parameter uncertainties, and high fault-tolerance capability under rotor and stator current sensor faults. In [17], also a new fault-tolerant control (FTC) strategy for a DFIG-based wind turbine with sensor fault is proposed. The DFIG system is decomposed into stator, rotor, grid current models, and the sensor fault observer is presented to provide accurate estimations of sensor fault components in the presence of model uncertainties.

Recent years, artificial intelligence (AI) has also been researched for fault detection and diagnosis in wind turbines. Reference [18] presents an LSTM-based diagnosis method for multiple open-circuit switch faults of back-to-back converter in DFIG-based wind turbine system. Simulation studies demonstrate the effectiveness of the proposed method in classifying multiple open-circuit faults. In [19], a convolutional neural network (CNN) model is presented to learn features from frequency data directly and detect faults of gearboxes. In [20], a novel approach based on DNN model is proposed to the fault detection in a direct drive wind turbine. Reference [21] presents a probabilistic neural network to detect and classify short-circuit and open-circuit faults in real time.

Sliding mode control is a kind of robustness control method with chattering. In order to improve the sliding mode controller's performance, the constant velocity reaching law (CVRL) was proposed in [22]. This CVRL reduces the chattering of the system, but the response speed of the system also decreases. Reference [22] also designed an exponential reaching law (ERL). Compared with the CVRL, it eliminates the inter-

dependence between response speed and chattering. However, the robustness of the system cannot be guaranteed while the chattering is reduced. In [23], a new exponential reaching law (NERL) is proposed that allows chattering reduction on control input for a Multi-Input / Multi-Output (MIMO) modular robot arm while keeping high tracking performance of the controller in the steady-state regime. However, when the system is close to the sliding mode surface, the system still makes a particular control gain to do back and forth movement, which means the system will maintain constant amplitude oscillation near the origin. Reference [24] also proposed a NERL. The NERL based sliding mode control proves to be capable of reducing the system chattering phenomenon as well as accelerating the approaching process. However, its anti-interference ability is feeble.

In this paper, to solve the lack of the above reaching law, a new reaching law (NRL) is proposed. The NRL achieves the unification of rapidity, smoothness, and robustness. And then, the NRL is employed to the observation of the DFIG rotor current. The sliding mode observer (SMO) based on the NRL (NRL- SMO) has an excellent tracking effect and is more sensitive to DFIG electrical faults. Under three different electrical faults of wind turbines, the NRL–SMO can accurately detect and locate the fault.

The arrangement of this paper is as follows. Section 2 of this paper theoretically analyzes the proposed NRL and proves the related theorem. In Section 3, NRL–SMO is designed, and its stability and robustness are analyzed. Section 4 gives the optimal parameter selection scheme of NRL–SMO. In Section 5, NRL–SMO is applied on a DFIG simulink model, and real-time results are compared to conventional SMO. In Section 6, the conclusion of the entire paper will be provided.

2. Proposal and analysis of NRL

The NRL presented in this paper is as follows:

$$\dot{s} = -ks - \frac{\varepsilon e^{-\beta(t-\lambda(t))}}{\delta_0 + (1-\delta_0)e^{-\alpha\|s\|}}sign(s), \qquad (1)$$

$\lambda(t) = \begin{cases} 0 & (|e| \le f_\xi) \\ t & (|e| > f_\xi) \end{cases}$, e is the error between the estimated sliding mode value and the target value, f_ξ is the critical value of the steady-state error that the system can tolerate, k, α, β, ε are positive parameter and $k > \beta$, $\alpha \gg 1$, $0 < \delta_0 < 1$, $\|s\|$ represents the norm of s.

At the initial stage of the system, when the starting point is far from the sliding mode surface, $e^{-\beta(t-\lambda(t))} \to 1$, $e^{-\alpha\|s\|} \to 0$, $\dot{s} \to -ks - \frac{\varepsilon}{\delta_0}sign(s)$. It guarantees that the state of the sliding mode system can approach the sliding mode at a higher speed at initial time. When the starting point is close to the sliding mode surface, $e^{-\beta(t-\lambda(t))} \to 1$, $e^{-\alpha\|s\|} \to 1$, $\dot{s} \to -\varepsilon sign(s)$. The state of the sliding mode system will slide up and down on the surface of the sliding mode. If ε is small, then the chattering due to the reaching law is weak.

2

Bull. Pol. Acad. Sci. Tech. Sci. 69(3) 2021, e137389

In the stabilization phase of the system with no interference, $|e| \leq f_\xi$, $\lambda(t) \rightarrow 0$. As time goes to infinity, $e^{-\beta(t-\lambda(t))} \rightarrow 0$, $\dot{s} \rightarrow 0$. This shows that the system chatter will also decay to zero in the form of an exponent.

In the stabilization phase of the system with interference, $|e| > f_\xi$, $\lambda(t) \rightarrow t$, $e^{-\beta(t-\lambda(t))} \rightarrow 1$, $e^{-\alpha\|s\|} \rightarrow 0$, the NRL switches to the form of the initial phase, $\dot{s} \rightarrow -ks - \dfrac{\varepsilon}{\delta_0} sign(s)$.

All of the above are optimal representations of NRL at different stages of the system. The properties of NRL are further explained in theorem 1 below.

Theorem 1.
1. The motion state will reach the sliding mode surface $s(t) = 0$ within a limited time t_r'.

$$t_r' < \frac{1}{k-\beta} \ln\left(1 + \frac{k-\beta}{\varepsilon}\|s(0)\|\right). \quad (2)$$

2. After the motion state reaching the sliding mode surface, the chattering decays exponentially to zero.

Proof.
1. Do not consider the system parameter uncertainty and external interference, the time function $\lambda(t) = 0$. In this case, the form of the NRL (1) will be:

$$\dot{s} = -ks - \frac{\varepsilon e^{-\beta t}}{\delta_0 + (1-\delta_0)e^{-\alpha\|s\|}} sign(s). \quad (3)$$

Assume:
$$N(s) = \frac{\varepsilon}{\delta_0 + (1-\delta_0)e^{-\alpha\|s\|}}.$$

When $\delta_0 \rightarrow 1$, then $N(s) = \varepsilon$. Equation (3) is transformed into:
$$\dot{s} = -ks - \varepsilon e^{-\beta t}. \quad (4)$$

Solve (4):

$$s(t) = s(0)e^{-kt} - \varepsilon \int_0^t e^{-k(t-\tau)}e^{-\beta\tau} sign\, s(\tau)\, d\tau. \quad (5)$$

Set the time that the sliding mode system reaches the sliding mode surface as t_e, when $\delta_0 \rightarrow 1$, then $s(t_e) = 0$, substitute it into (5):

$$0 = s(0)e^{-kt_e} - \varepsilon e^{-kt_e} sign\, s(0) \int_0^{t_e} e^{(k-\beta)\tau}\, d\tau,$$

$$0 = e^{-kt_e}\left[s(0) - \frac{\varepsilon}{k-\beta}\left(e^{(k-\beta)t_e} - 1\right) sign\, s(0)\right], \quad (6)$$

$$s(0) = \frac{\varepsilon}{k-\beta}\left(e^{(k-\beta)t_e} - 1\right) sign\, s(0).$$

Introduce
$$s^T sign\, s = \|s\|_1 \geq \|s\|_2, \quad (7)$$

where $\|s\|_1$ is the first norm of s, $\|s\|_2$ is the second norm of s.

Multiply $sign^T s(0)$ on both sides of (6), from the (7), we have:

$$\|s(0)\| \geq \frac{\varepsilon}{k-\beta}\left(e^{(k-\beta)t_e} - 1\right),$$

$$t_e \leq \frac{1}{k-\beta} \ln\left(1 + \frac{k-\beta}{\varepsilon}\|s(0)\|\right).$$

When $0 < \delta_0 < 1$

$$0 < \delta_0 + (1-\delta_0)e^{-\alpha\|s\|} < 1,$$

$$N(s) > \varepsilon,$$

we have the arrival time t_r':

$$t_r' < \frac{1}{k-\beta} \ln\left(1 + \frac{k-\beta}{N(s)}\|s(0)\|\right) < t_e,$$

$$t_r' < \frac{1}{k-\beta} \ln\left(1 + \frac{k-\beta}{\varepsilon}\|s(0)\|\right).$$

2. Take $s \rightarrow 0$ on both sides of (3):

$$\left.\frac{ds}{dt}\right|_{s\rightarrow 0} = -ks|_{s\rightarrow 0} - \left.\frac{\varepsilon e^{-\beta t}}{\delta_0 + (1-\delta_0)e^{-\alpha\|s\|}} sign(s)\right|_{s\rightarrow 0}.$$

Then:
$$\frac{ds}{dt} \rightarrow -\varepsilon e^{-\beta t} sign(s).$$

With $t \rightarrow \infty$:
$$\frac{ds}{dt} \rightarrow 0.$$

Thus, the chatter will decay to zero exponentially.

3. Rotor current NRL–SMO for DFIG

Aiming at the fault detection of DFIG, the proposed NRL is applied to design a SMO that can adapt to sudden faults. Through the NRL–SMO, various states of the rotor current of the DFIG stably tracked and the change curve analysis of the sliding mode control law is performed to achieve the purpose of fault detection.

3.1. The design of rotor current NRL–SMO for DFIG.
In this paper, a three-phase asynchronous motor with a wound rotor is used as a DFIG. Figure 1 shows the control structure diagram of the sliding mode observer-based on stator voltage orientation for DFIG.

The correlation between the stator current and the rotor current can be obtained after decoupling the stator current and the rotor current through the vector control method of stator flux

Bull. Pol. Acad. Sci. Tech. Sci. 69(3) 2021, e137389

3

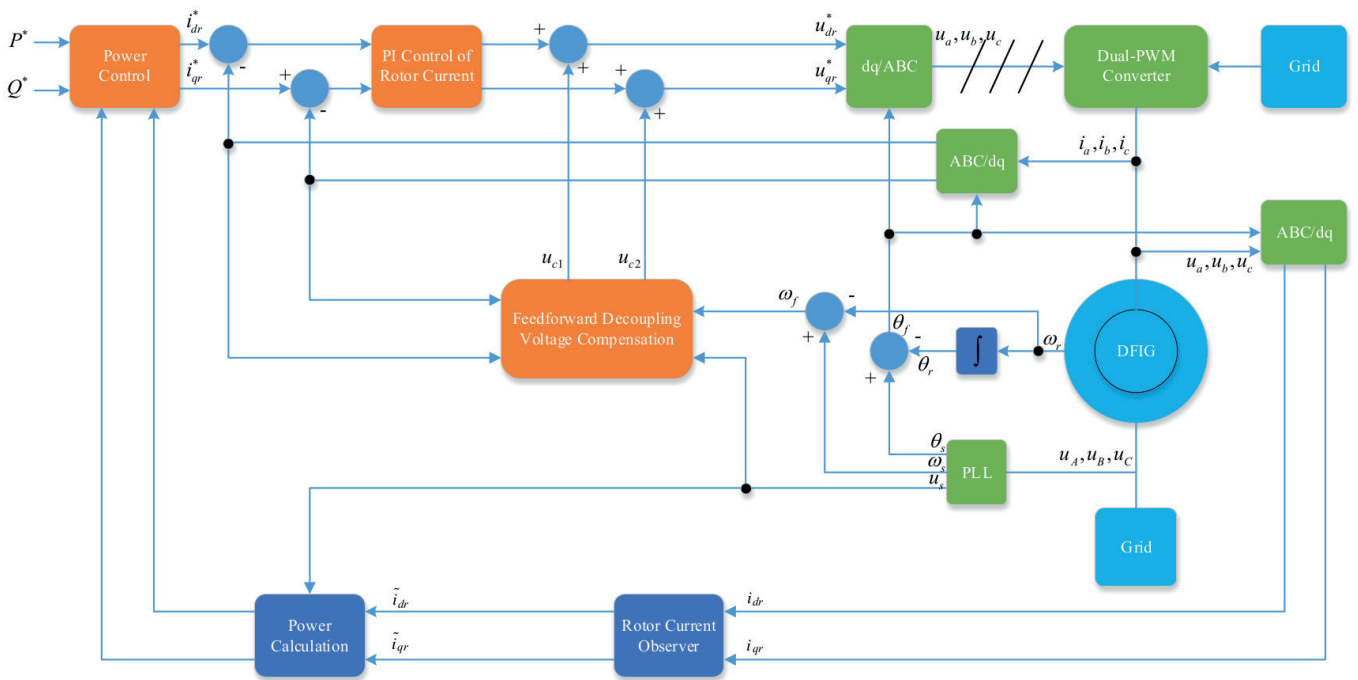R.Q. Li, W.X. Yu, J.N. Wang, Y. Lu, D. Jiang, G.L. Zhong, and Z.B. Zhou

Fig. 1. DFIG control structure diagram of sliding mode observer for stator voltage orientation

orientation. At this time, we obtain the rotor side mathematical model of doubly-fed induction motor [25]:

$$
\begin{cases}
\begin{bmatrix} \dot{i}_{dr} \\ \dot{i}_{qr} \end{bmatrix} = A_0 \begin{bmatrix} i_{dr} \\ i_{qr} \end{bmatrix} + A_1 \begin{bmatrix} \dfrac{-L_m i_{qr}}{L_s} \\ \dfrac{\varphi_s - L_m i_{dr}}{L_s} \end{bmatrix} + Bu, \\
y = C i_r,
\end{cases} \tag{8}
$$

where

$$
A_0 = \frac{1}{\sigma} \cdot \begin{bmatrix} \dfrac{-R_r}{L_r} & \omega_f - \dfrac{\omega_s L_m^2}{L_s L_r} \\ \dfrac{\omega_s L_m^2}{L_s L_r} - \omega_f & \dfrac{-R_r}{L_r} \end{bmatrix},
$$

$$
A_1 = \begin{bmatrix} \dfrac{R_s L_m}{\sigma L_s L_r} & \dfrac{\omega_f - \omega_s}{\sigma L_r} L_m \\ \dfrac{\omega_s - \omega_f}{\sigma L_r} L_m & \dfrac{R_s L_m}{\sigma L_s L_r} \end{bmatrix},
$$

$$
B = \begin{bmatrix} -\dfrac{L_m}{\sigma L_s L_r} & 0 & \dfrac{1}{\sigma L_r} & 0 \\ 0 & -\dfrac{L_m}{\sigma L_s L_r} & 0 & \dfrac{1}{\sigma L_r} \end{bmatrix},
$$

$$
C = \begin{bmatrix} 1 & 0 \\ 0 & 1 \end{bmatrix},
$$

i_{dr}, i_{qr} are the current vectors of the rotor of the d, q; R_s, R_r are rotor and stator resistance; L_s, L_r are the self-inductance of

the stator and rotor; L_m is the mutual inductance between the stator and the rotor; ω_s, ω_f are the stator speed and slip speed

$$
\sigma = 1 - \frac{L_m^2}{L_s L_r}.
$$

Simplify (8) into (9):

$$
\begin{cases}
\dot{i}_r = A i_r + Bu + f, \\
y = C i_r,
\end{cases} \tag{9}
$$

where

$$
A = \begin{bmatrix} -\dfrac{R_s L_m^2}{\sigma L_s^2 L_r} - \dfrac{R_r}{\sigma L_r} & \omega_f \\ -\omega_f & -\dfrac{R_s L_m^2}{\sigma L_s^2 L_r} - \dfrac{R_r}{\sigma L_r} \end{bmatrix},
$$

$$
B = \begin{bmatrix} -\dfrac{L_m}{\sigma L_s L_r} & 0 & \dfrac{1}{\sigma L_r} & 0 \\ 0 & -\dfrac{L_m}{\sigma L_s L_r} & 0 & \dfrac{1}{\sigma L_r} \end{bmatrix},
$$

$$
f = \begin{bmatrix} \dfrac{\omega_f - \omega_s}{\sigma L_r L_s} L_m \psi_s \\ \dfrac{R_s L_m \psi_s}{\sigma L_s^2 L_r} \end{bmatrix}.
$$

According to sliding mode variable structure control and state observer theory, the structure of the SMO is constructed as follows:

$$
\begin{cases}
\dot{\tilde{i}}_r = A \tilde{i}_r + Bu + f + \tilde{v}, \\
y = C \tilde{i},
\end{cases} \tag{10}
$$

4

Bull. Pol. Acad. Sci. Tech. Sci. 69(3) 2021, e137389

where $\tilde{i}_r = \begin{bmatrix} \tilde{i}_{dr} & \tilde{i}_{qr} \end{bmatrix}^T$ is the estimated value of the rotor current and $\tilde{v}$ is the control law of the sliding mode observer, $\tilde{v} = \begin{bmatrix} v_1 & v_2 \end{bmatrix}^T$.

The design sliding surface is:

$$s = \{e : ce = 0\}, \tag{11}$$

$$e = \begin{bmatrix} e_1 \\ e_2 \end{bmatrix} = \begin{bmatrix} i_{dr} - \tilde{i}_{dr} \\ i_{qr} - \tilde{i}_{qr} \end{bmatrix},$$

c is the sliding mode surface parameter, $c > 0$.

From (9), (10) and (11), we can get:

$$\dot{s} = cA\left(i_r - \tilde{i}_r\right) - c\tilde{v}. \tag{12}$$

Combined with the NRL proposed in (1), the sliding mode control law can be obtained:

$$\tilde{v} = \begin{bmatrix} v_1 \\ v_2 \end{bmatrix} = Ae - \frac{1}{c}\dot{s}$$

$$= A \begin{bmatrix} e_1 \\ e_2 \end{bmatrix}$$

$$- \frac{1}{c}\left(-ks - \frac{\varepsilon e^{-\beta(t-\lambda(t))}}{\delta_0 + (1-\delta_0)e^{-\alpha\|s\|}} \operatorname{sign}(s) \right). \tag{13}$$

Substitute (13) into (10) to get the complete mathematical model of the rotor current NRL–SMO:

$$\begin{cases} \dot{\tilde{i}}_r = A\tilde{i}_r + Bu + f + A\left[i_r - \tilde{i}_r\right] \\ \quad - \frac{1}{c}\left(-ks - \frac{\varepsilon e^{-\beta(t-\lambda(t))}}{\delta_0 + (1-\delta_0)e^{-\alpha\|s\|}} \operatorname{sign}(s) \right), \\ y = C\tilde{i}. \end{cases} \tag{14}$$

3.2. Stability analysis of NRL–SMO. In order to illustrate that the system of the rotor current NRL–SMO (14) is asymptotically stable, the following will prove it by Lyapunov stability theory, and get Theorem 2.

Theorem 2. For the system of rotor current NRL–SMO (14), the system gradually stabilizes under the action of the sliding mode control law (13).

Proof. Define the Lyapunov function:

$$V = \frac{1}{2}s^T \cdot s. \tag{15}$$

Substitute (9), (10), (11), (12) into the derivative of the Lyapunov function:

$$\dot{V} = \dot{s}^T s + s^T \dot{s}$$

$$= \begin{bmatrix} \dot{s}_1 & \dot{s}_2 \end{bmatrix} \begin{bmatrix} s_1 \\ s_2 \end{bmatrix} + \begin{bmatrix} s_1 & s_2 \end{bmatrix} \begin{bmatrix} \dot{s}_1 \\ \dot{s}_2 \end{bmatrix}$$

$$= 2\left(\dot{s}_1 s_1 + \dot{s}_2 s_2\right)$$

$$= 2\left[c\left(-\frac{R_s L_m^2}{\sigma L_s^2 L_r} - \frac{R_r}{\sigma L_r} \right)\left(i_{dr} - \tilde{i}_{dr}\right)s_1 + c\omega_f\left(i_{qr} - \tilde{i}_{qr}\right)s_1 \right.$$

$$- c\left(-\frac{R_s L_m^2}{\sigma L_s^2 L_r} - \frac{R_r}{\sigma L_r} \right)\left(i_{dr} - \tilde{i}_{dr}\right)s_1 - c\omega_f\left(i_{qr} - \tilde{i}_{qr}\right)s_1$$

$$- ks_1^2 - \frac{\varepsilon e^{-\beta(t-\lambda(t))}}{\delta_0 + (1-\delta_0)e^{-\alpha\|s\|}} \operatorname{sign}(s_1)s_1 + c(-\omega_f)$$

$$\times \left(i_{dr} - \tilde{i}_{dr}\right)s_2 + c\left(-\frac{R_s L_m^2}{\sigma L_s^2 L_r} - \frac{R_r}{\sigma L_r} \right) \times \left(i_{qr} - \tilde{i}_{qr}\right)s_2$$

$$- c(-\omega_f)\left(i_{dr} - \tilde{i}_{dr}\right)s_2 - c\left(-\frac{R_s L_m^2}{\sigma L_s^2 L_r} - \frac{R_r}{\sigma L_r} \right)\left(i_{qr} - \tilde{i}_{qr}\right)$$

$$\left. \times s_2 - ks_2^2 - \frac{\varepsilon e^{-\beta(t-\lambda(t))}}{\delta_0 + (1-\delta_0)e^{-\alpha\|s\|}} \operatorname{sign}(s_2)s_2 \right]$$

$$= 2\left[-ks_1^2 - \frac{\varepsilon e^{-\beta(t-\lambda(t))}}{\delta_0 + (1-\delta_0)e^{-\alpha\|s\|}}|s_1| \right.$$

$$\left. - ks_2^2 - \frac{\varepsilon e^{-\beta(t-\lambda(t))}}{\delta_0 + (1-\delta_0)e^{-\alpha\|s\|}}|s_2| \right].$$

Since k, α, β, δ_0 are positive parameters, then $\dot{V} \leq 0$ known by Lyapunov's stability theorem, the rotor current NRL–SMO is asymptotically stable.

3.3. Robust analysis of the rotor current NRL–SMO. To make the rotor current NRL–SMO can track the rotor current in different states stably, it is necessary to analyze the robustness of the rotor current NRL–SMO.

Theorem 3. For the system of rotor current with uncertainty interference, as shown in (16), when $d(t) < \dfrac{\varepsilon}{c\delta_0}$, under the action of sliding mode control law, NRL–SMO system is still stable, that is, NRL–SMO system will still gradually converge to the sliding mode surface $s(t) = 0$.

Proof. Consider the following DFIG rotor-side control system with uncertain interference:

$$\begin{cases} i_r = Ai_r + Bu + f + d(t), \\ y = Ci_r \end{cases} \tag{16}$$

$d(t)$ represents the uncertain interference or unknown part of the system, assuming that the following matching conditions are met:

$$\operatorname{rank}(d(t)) = \operatorname{rank}(i_r(t)), \quad \|d(t)\| \leq d_M, \tag{17}$$

where d_M is a positive number.

Bull. Pol. Acad. Sci. Tech. Sci. 69(3) 2021, e137389

5

The rotor current NRL–SMO is as in (14), then it is obtained by subtracting (14) from (16):

$$\dot{s} = c\dot{e}$$
$$= cA\left(i_r - \tilde{i}_r\right) + cd(t) - cA\left(i_r - \tilde{i}_r\right)$$
$$+ c\frac{1}{c}\left(-ks - \frac{\varepsilon e^{-\beta(t-\lambda(t))}}{\delta_0 + (1-\delta_0)e^{-\alpha\|s\|}}sign(s)\right), \qquad (18)$$

$$\dot{s} = cd(t) - ks - \frac{\varepsilon e^{-\beta(t-\lambda(t))}}{\delta_0 + (1-\delta_0)e^{-\alpha\|s\|}}sign(s). \qquad (19)$$

According to the Lyapunov function, the arrival condition for sliding mode is $s^T\dot{s} < 0$, then multiply s^T on both sides of (19):

$$s^T\dot{s} = s^T\left(Gd(t) - ks - \frac{\varepsilon e^{-\beta(t-\lambda(t))}}{\delta_0 + (1-\delta_0)e^{-\beta\|s\|}}sign(s)\right),$$

$$s^T\dot{s} \leq c\|s\|d_M - k\left(s_1^2 + s_2^2\right) - \frac{\varepsilon e^{-\beta(t-\lambda(t))}}{\delta_0 + (1-\delta_0)e^{-\beta\|s\|}} \times (|s_1| + |s_2|).$$

When

$$\frac{\varepsilon e^{-\beta(t-\lambda(t))}}{\delta_0 + (1-\delta_0)e^{-\beta\|s\|}} > cd_M,$$

$s^T\dot{s} < 0$. Because of the uncertainty interference in the system, the time function $\lambda(t) \to t$:

$$\frac{\varepsilon e^{-\beta(t-\lambda(t))}}{\delta_0 + (1-\delta_0)e^{-\beta\|s\|}} \to \frac{\varepsilon}{\delta_0}.$$

And when:
$$d_M < \frac{\varepsilon}{c\delta_0},$$

$s^T\dot{s} < 0$. The system stability condition is satisfied, that is, NRL–SMO system will still gradually converge to the sliding mode surface $s(t) = 0$.

4. Parameters selection of Rotor current NRL–SMO and decision method of the time function

4.1. Parameters selection of Rotor current NRL–SMO

4.1.1. Parameter k, β.
From Theorem 1, the time for the system state to reach the sliding surface meets the following conditions:

$$t_r' < \frac{1}{k-\beta}\ln\left(1 + \frac{k-\beta}{\varepsilon}\|s(0)\|\right).$$

Assume: $z = k - \beta$

$$t_r' < y(z) = \frac{1}{z}\ln\left(1 + \frac{\|s(0)\|}{\varepsilon}\right).$$

Derivative of function y with respect to z:

$$y'(z) = \frac{\dfrac{\frac{1}{\varepsilon}}{\frac{\|s(0)\|z}{\varepsilon} + 1} - \ln\left(1 + \frac{\|s(0)\|}{\varepsilon}z\right)}{z^2},$$

$$y'(z) = \frac{\dfrac{\left(\frac{\|s(0)\|}{\varepsilon}z\right)}{1 + \frac{\|s(0)\|}{\varepsilon}z} - \ln\left(1 + \frac{\|s(0)\|}{\varepsilon}z\right)}{z^2}.$$

Because of $k > \beta$, we know:

$$\frac{\frac{1}{\varepsilon}}{\frac{\|s(0)z\|}{} + 1} < 1.$$

When

$$z > \frac{\varepsilon(e-1)}{\|s(0)\|}, \quad \ln\left(1 + \frac{\|s(0)\|}{\varepsilon}z\right) > 1,$$

$$y'(z) < 0.$$

The function $y(z)$ decreases monotonously, so in order to improve the system response speed, we can increase the value of $z = k - \beta$.

4.1.2. Parameter α.
The parameter α is in the exponential switching function $(1-\delta_0)e^{-\alpha\|s\|}$. When the state of the sliding mode system is far away from the sliding mode surface, in order to get a fast response speed, the exponential switching function should satisfy $e^{-a\|s\|} \to 0$, parameter a should satisfy $a \gg 1$.

4.1.3. Parameter ε, δ_0.
From Section 2, we know that when the system state is far from the sliding surface, $\dot{s} \to -ks - \frac{\varepsilon}{\delta_0}sign(s)$, so the value of $\frac{\varepsilon}{\delta_0}$ should be large to ensure the response speed of the system; When the system state is close to the sliding surface, $\dot{s} \to -\varepsilon sign(s)$, ε cannot be too large, otherwise it will produce higher chattering. In order to satisfy the condition that $\frac{\varepsilon}{\delta_0}$ is a large number and δ_0 is a small number at the same time, parameter δ_0 should satisfy $\delta_0 \leq 1$.

4.1.4. Parameter c.
From Section 3.3, we know that when the boundary of uncertain interference satisfies $d_M < \frac{\varepsilon}{\delta_0}$, the sliding mode system is stable. Therefore, parameter affects the robustness of the sliding mode observer system. We can improve the robustness of the system by reducing the value of parameter c.

4.1.5. Summary.
From the above analysis, we can find that the system response time and stability not only depend on the influence of various parameters, but also depend on the initial value $\|s(0)\|$ of the system and the boundary value d_M of uncertain interference. Therefore, we cannot determine the specific

6

Bull. Pol. Acad. Sci. Tech. Sci. 69(3) 2021, e137389

parameters of NRL–SMO but can only give a rough selection range of each parameter.

4.2. Decision method of the time function.

From the analysis of the robustness of the sliding mode observer system in Section 3.3, we know that the time function $\lambda(t)$ is mainly to improve the robustness of the system during the fault phase. For the time function to work, the residual e and the critical values of steady-state errors f_ξ must be introduced, The size of f_ξ is determined by the steady-state error that meets the requirements of the system $f_\xi > 0$.

When the difference $|e|$ between the actually detected rotor current and the sliding mode estimate is greater than f_ξ, $\lambda(t) \to t$. The purpose of eliminating the time t in the time exponential term in the sliding mode observer and increasing the robustness of the sliding mode system are achieved. When $|e| < f_\zeta$, $\lambda(t) \to 0$, the time function $\lambda(t)$ does not work.

5. Fault design and simulation analysis

This section uses MATLAB / SIMULINK to build a vector-controlled DFIG model. On this basis, a rotor current NRL–SMO is built. Then three common wind turbine system faults are given: DFIG inter-turn stator fault, grid voltage drop fault, and rotor current sensor fault. The feasibility of the proposed sliding mode observer is verified by observing the estimation error of the rotor current output of the sliding mode system at different fault stages. By following the output estimation error of the rotor current SMO based on different reaching law, it is verified that NRL–SMO is superior to the SMO based on ERL in tracking the rotor current state. Finally, analyzing the change curve of the sliding mode control law to achieve the purpose of fault detection. Table 1 are the parameters of the wind turbine to be simulated in this paper.

Table 1
Main parameters of the DFIG system

Item	Value	Item	Value
Grid voltage (V)	220	Nominal power (VA)	3730
Grid frequency (Hz)	50	Voltage (line-line) (V)	460
DC Bus Voltage	600	Pole pairs	4
Wind speed m/s	< 12	$R_s(\Omega)$	1.115
Blade radius of wind turbine (m)	2	$R_r(\Omega)$	1.083
Gear box transmission ratio	1:3	$L_{\sigma s}, L_{\sigma r}$ (mH)	5.974
		L_m (H)	0.2037

Using the selection rules of the NRL parameters described in Section 4 and the decision method of time function, combined with the parameters of the DFIG system shown in Table 1, the parameters of the SMO based on NRL are $c = 0.1$, $k = 100$, $\varepsilon = 10$, $\beta = 0.05$, $\delta_0 = 0.001$, $\alpha = 15$, $f_\xi = 0.1$. The parameters of the SMO based on ERL are $k = 100$, $\varepsilon = 100$.

5.1. Unfaulty conditions.

The system simulation duration is 3 s. When the DFIG system is running in a healthy state, the wind speed set at 0–1 s is 6 m/s, the wind speed at 1–2 s is 8 m/s, and the wind speed returns to 6 m/s after 2 s. Figure 2 is the given wind speed curve.
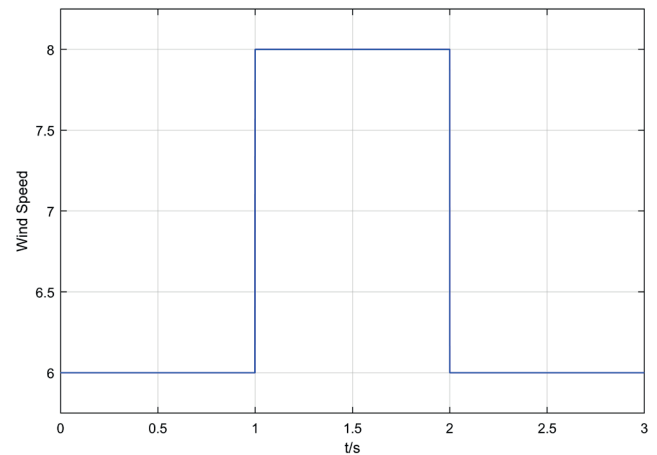

Fig. 2. Wind speed curve

Figure 3 is the tracking curve of the actual measured value of the rotor current d-axis and the estimated value of the sliding mode observer. Figure 4 is the error curve of the real measured value of the rotor current d-axis and the estimated value of the sliding mode. Figures 3 and 4 show that the NRL–SMO can accurately track the state of the d-axis of the rotor current during the initial stage of the system or the stage of variable wind speed. The sliding mode observer based on the ERL can hardly track the rotor current state of the system at the above step, and the error can be up to 80 A.
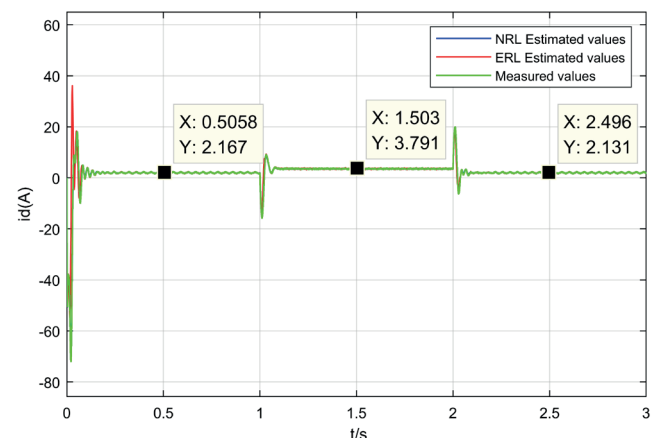

Fig. 3. Rotor current d-axis measurement and estimated value tracking curve

It can be found from Fig. 4 that when the system is in a stable state, both SMO can track the rotor current state of the system. The error of the NRL–SMO is steady at about 0.003 A, and almost, chattering does not occur, but SMO based on the ERL will produce a sliding mode modal region of $-0.01 \sim 0.01$ A.
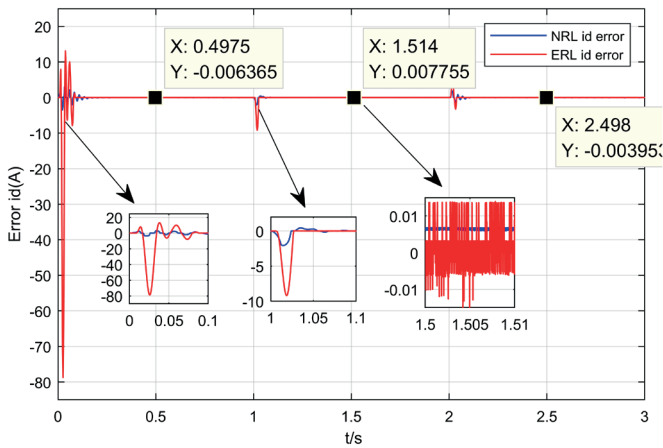
Bull. Pol. Acad. Sci. Tech. Sci. 69(3) 2021, e137389

7

R.Q. Li, W.X. Yu, J.N. Wang, Y. Lu, D. Jiang, G.L. Zhong, and Z.B. Zhou

Fig. 4. Error curve of rotor current *d*-axis measured value and estimated value

Figures 5 and 6 are the tracking curve and error curve of the actual measured value and sliding mode estimated value of the system rotor current q-axis, respectively, and the same conclusion as the d-axis can be obtained from the figure. Figures 7 and 8 are the variable curves of the sliding mode control law based on the NRL and the ERL, respectively. It can be seen from the figure that the maximum value of the new sliding mode control law can reach 20000 at the initial stage of the system. The value of the traditional sliding mode control law does not exceed 10000, which shows that the new SMO responds more sensitively to the initial error and responds faster. When the system is stable, the amplitude of the new sliding mode control law does not exceed 103. In contrast, the traditional sliding mode control law can reach 1000. It is indicating that the observation error and the system chatter generated by the new sliding mode control law in the stable stage are small. When the system is in the variable wind speed stage of 1 and 2 s, the values of the two sliding mode control laws have reached about 1300, which shows that the two sliding mode control laws can recognize the system's change wind speedwell. Moreover, the change frequency of the two sliding mode control laws in the variable
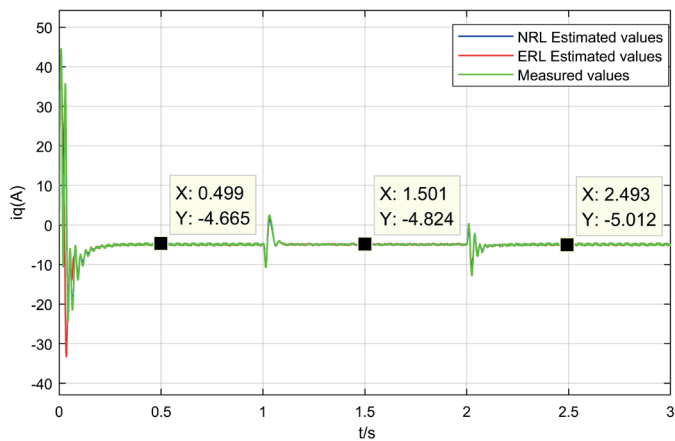
wind speed stage is far lower than the steady-state of the system, which can be used as a performance index for judging the condition of the wind speed of the system.
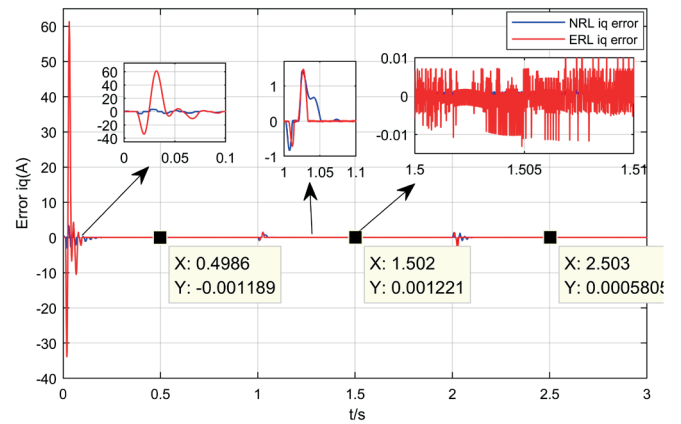
Fig. 6. Error curve of measured and estimated values of rotor current *q*-axis
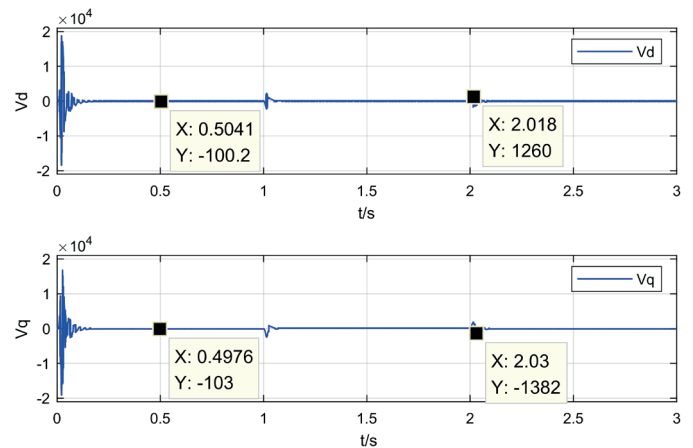
Fig. 7. Variation curve of sliding mode control law based on the NRL-current *q*-axis
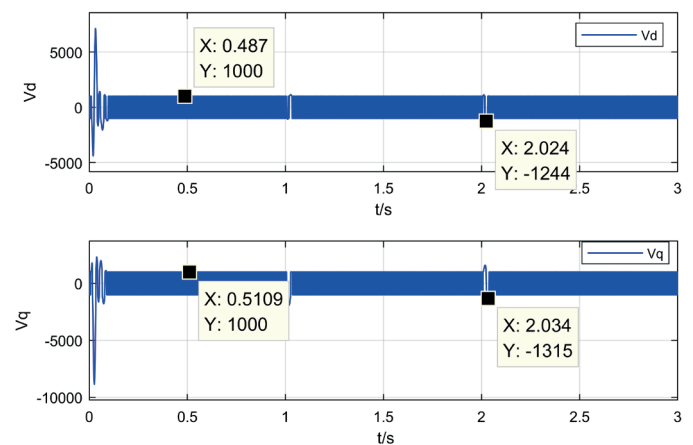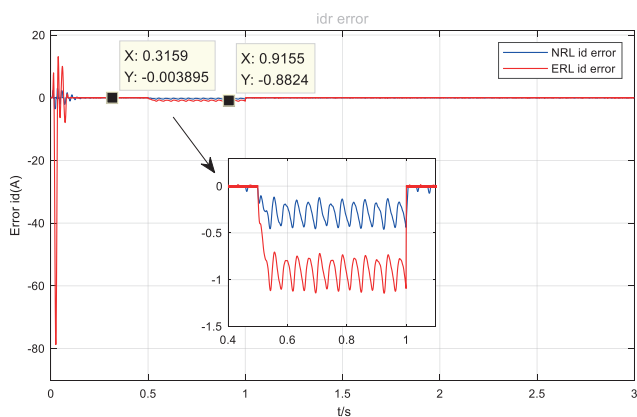

Fig. 5. Rotor current *q*-axis measured value and estimated value tracking curve

Fig. 8. Variation curve of sliding mode control law based on the ERL

8

Bull. Pol. Acad. Sci. Tech. Sci. 69(3) 2021, e137389

5.2. Inter-turn stator fault. During the operation of the DFIG, the turns of the motor winding often fail due to various overvoltage damages or wire quality problems. The following model is designed to simulate this fault. ΔR_s is the change value of the short-circuit fault resistance of the stator inter-turn fault. The expression of resistance fault change set in this paper is as (20):

$$\Delta R_s = \begin{cases} 0 & 0 \le t \le 0.5 \\ -0.1115 & 0.5 < t < 1.0 \\ 0 & t \ge 1.0 \end{cases}. \qquad (20)$$

Figure 9 is the tracking curve of the actual measured value of the rotor current d-axis and the estimated value of the sliding mode observer; Fig. 10 is the error curve of the actual measured value of the rotor current d-axis and the estimated value of the sliding mode. It can be seen from Fig. 9 that when the system fails in 0.5 s, the rotor current fluctuates very little. It can be seen from Fig. 10, After the failure, the observation error of SMO–NRL rose from about 0.003 A to about –0.5 A, and the observation error of SMO–ERL rose to about 1.1 A, indicating that the fault caused damage to the observer system and made the residual error not zero. Both observers can detect the occurrence of the fault.
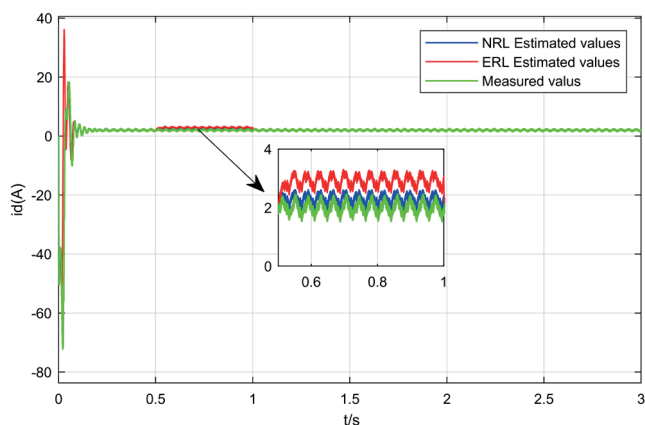
Fig. 9. Rotor current *d*-axis measurement and estimated value tracking curve

Fig. 10. Error curve of rotor current *d*-axis measured value and estimated value

Figures 11 and 12 are the tracking curve and error curve of the actual measured value and sliding mode estimated value of the system rotor current q-axis, respectively, and the same conclusion as the d-axis can be obtained from the figure. Figures 13 and 14 are the change curves of the sliding mode control law based on the NRL and the ERL when the Inter-turn stator fault occurs. In the fault phase (0.5–1.0 s) the value of the new
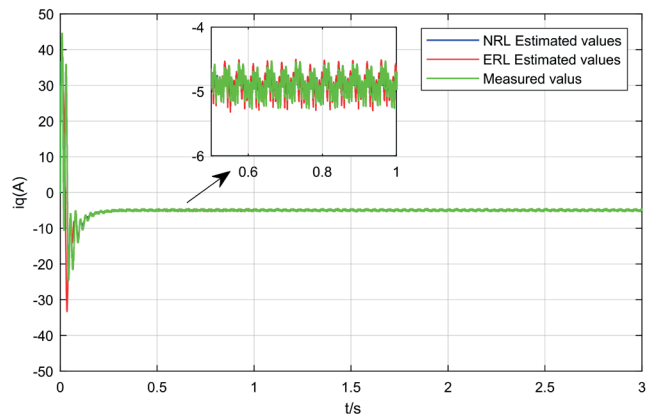

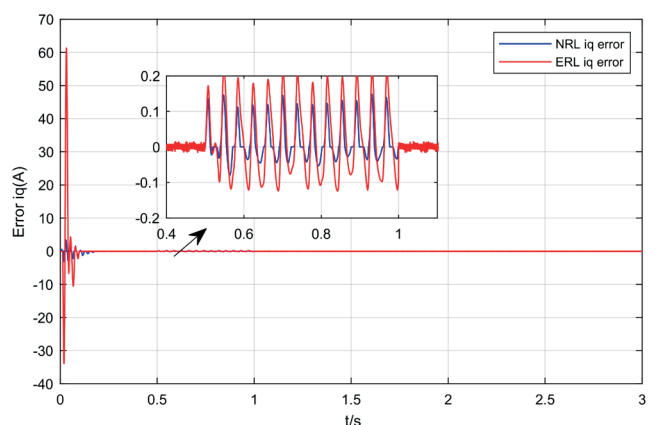Fig. 11. Rotor current *q*-axis measured value and estimated value

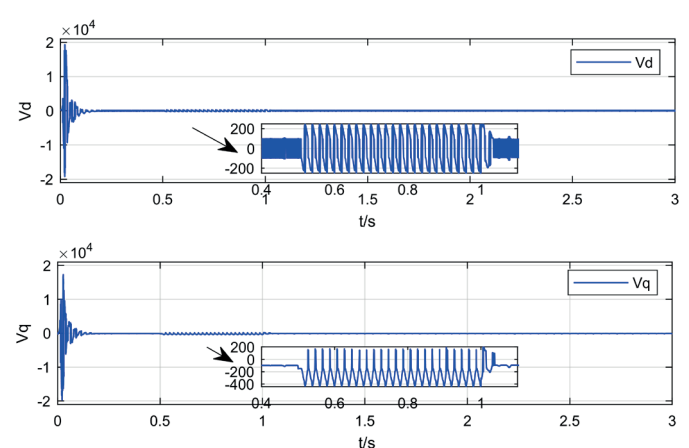Fig. 12. Error curve of measured and estimated values of rotor current *q*-axis

Fig. 13. Variation curve of sliding mode control law based on the NRL

sliding mode control law will rise from 100 to 200, while the value of the traditional sliding mode control law will be maintained at 1000. This indicates that NRL–SMO is more sensitive to failures, while ERL–SMO cannot identify inter-turn stator fault through changes in the control law.
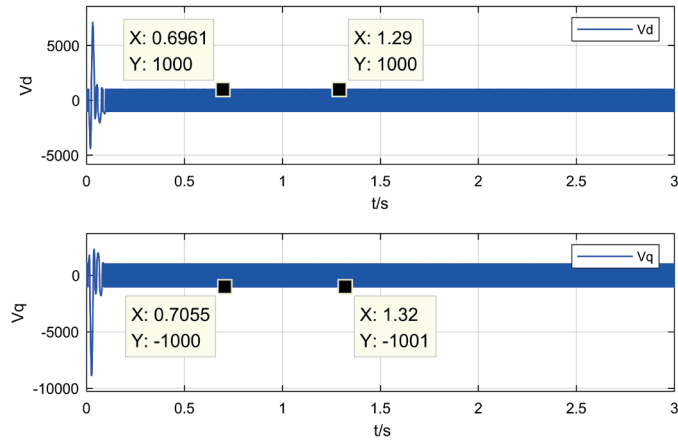

Fig. 14. Variation curve of sliding mode control law based on the ERL

5.3. Grid voltage drop fault. Voltage drop fault is a kind of fault that is more harmful to the wind turbine system in practice. The following article simulates this kind of fault on the simulation software through its physical meaning. It observes the tracking status of the sliding mode observer when the wind turbine system suffers from the grid fall fault.

In this paper, the voltage amplitude value at the input end of the power grid is set to 311 V, the frequency is 50 Hz, and the phase difference of the three-phase voltage is 120 degrees. The wind turbine system is set to drop the three-phase voltage on the grid side during 0.5 s to 1 s. After 1s, the grid voltage returns to the standard value. Because the symmetrical three-phase voltage drops, the corresponding voltage amplitude will also drop. In the static space coordinate system, the space vector expression can be expressed by (21):

$$u_g = U_g(1-h)e^{j\omega_g t}. \tag{21}$$

In Eq. (21), U_g is the grid voltage amplitude, w_g is the grid voltage electrical angular velocity, and h is the percentage indicating the degree of fault.

Figure 15 is the tracking curve of the actual measured value of the rotor current d-axis and the estimated value of the sliding mode observer; Fig. 16 is the error curve of the actual measured value of the rotor current d-axis and the estimated value of the sliding mode. The figure shows that during the fault phase and the system recovery phase, the rotor current will fluctuate violently, and the error between the estimated value and the actual value of the two sliding mode observers will increase. The error of SMO based on ERL can be up to 56.53 A. However, the error based on the NRL–SMO in this paper does not exceed 3.253 A. It can be seen from the enlarged view of the error curve of Fig. 16 in 2–2.5 s. At this stage, the performance of

the new sliding mode observer is not as good as that of the traditional sliding mode. However, when the system is completely stable at 2.8 s, the error is stable at 0.003, and the sliding mode is much smaller than the traditional sliding mode observer. The above shows that NRL–SMO has a stronger anti-interference ability and less chattering.
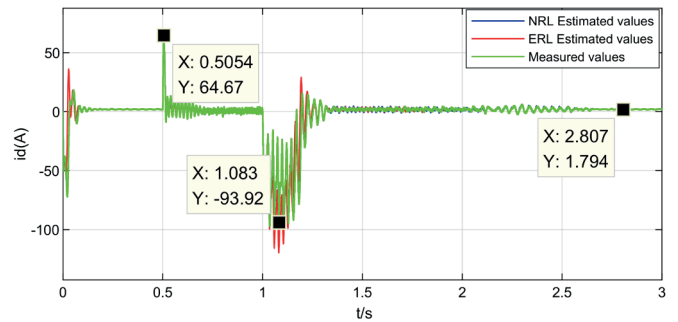

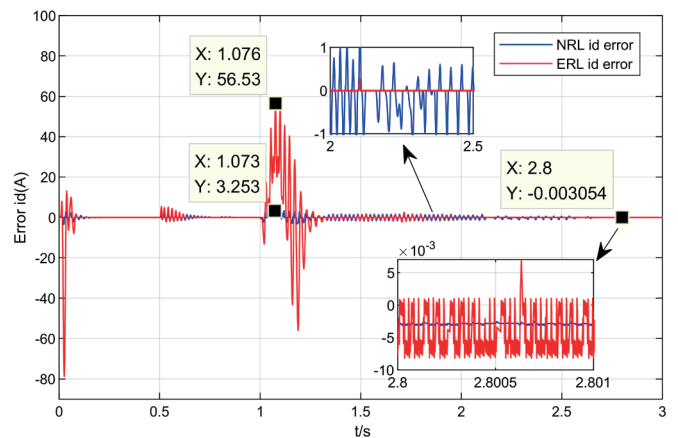Fig. 15. Rotor current d-axis measurement and estimated value tracking curve

Fig. 16. Error curve of rotor current d-axis measured value and estimated value

Figures 17 and 18 are the tracking curve and error curve of the actual measured value and sliding mode estimated value of the system rotor current q-axis, respectively, and the same conclusion as the d-axis can be obtained from the figure. Figures 19 and 20 are the change curves of the sliding mode control law based on the NRL and the ERL when the grid voltage drop fault occurs. It can be seen from the figure that in the fault phase (0.5–1 s), the new sliding mode control law will increase sharply but will soon return to a relatively low mode, and the traditional sliding mode control law is not sensitive enough. During the system recovery phase, the sliding mode control law fluctuates greatly. The maximum value of the new sliding mode control law reaches 16520, the maximum value of the traditional sliding mode control law reaches 7854, and the two continue for a long time. After 1.5 s, the mode of the new control law is still in. It is continuously shrinking, and the traditional control law is almost unchanged. The above also shows that the

new observer has a more sensitive response, stronger robustness, higher requirements for system error and chatter, and can pass the frequency, amplitude, and Time to judge whether the voltage drop fault occurs in the DFIG system.
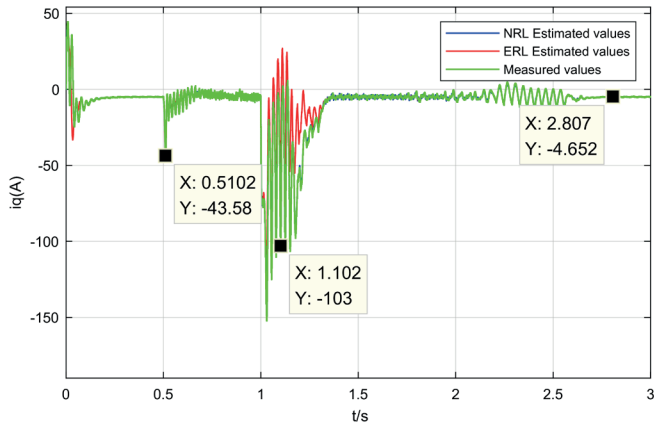

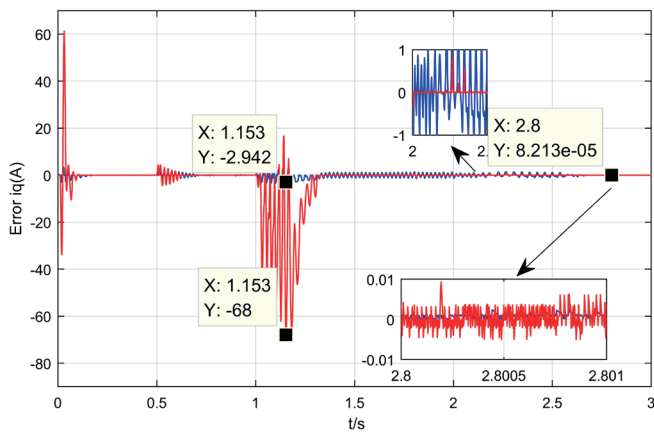Fig. 17. Rotor current q-axis measured value and estimated value tracking curve

Fig. 18. Error curve of rotor current q-axis measured value and estimated value
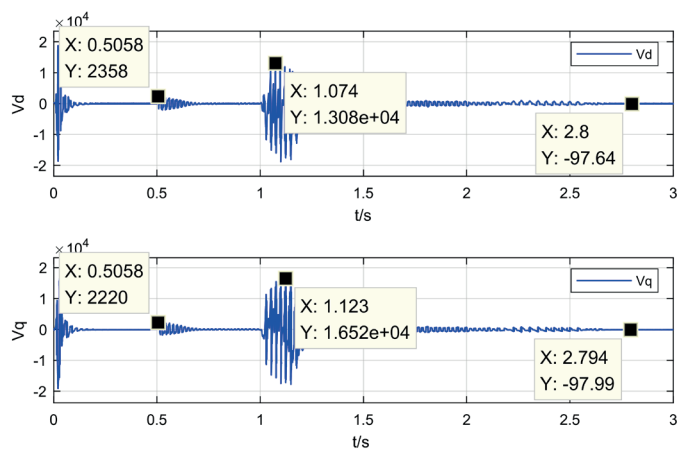

Fig. 19. Variation curve of sliding mode control law based on the NRL
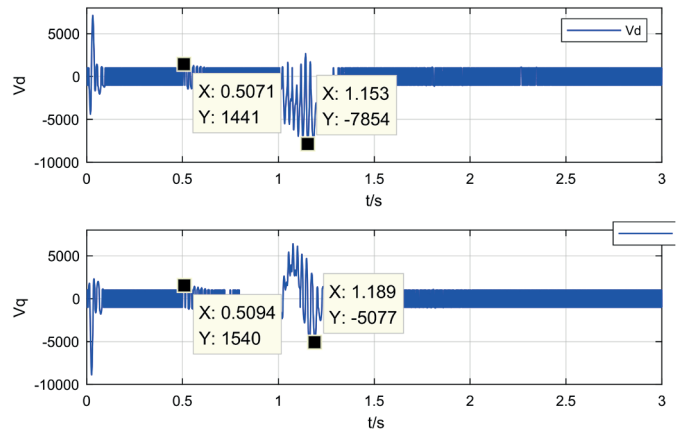

Fig. 20. Variation curve of sliding mode control law based on the ERL

5.4. Rotor current sensor fault. Rotor current sensor fault is also a common failure in actual production. It occurs at the output of the system, and it is easy to control and solve, so it is essential to discuss. The value of fault value A is shown in (22):

$$\Delta R_s = \begin{cases} 0 & 0 \le t \le 0.5 \\ 4e^{\sin(\pi t)} & 0.5 \le t < 1.0 \\ 0 & t \ge 1.0 \end{cases} \tag{22}$$

Figure 21 is estimated value of the sliding mode observer; Fig. 22 is the error curve of the actual measured value of the rotor current d-axis and the estimated value of the sliding mode. It can be seen from the figure that when the sensor fails, the SMO based on the ERL can't follow the actual measurement value of the rotor current d-axis during the fault phase, and the maximum error can reach 10.35 A. The error between the estimated value of the NRL–SMO and the actual measured value of the sensor remains near 0.1 A, which indicates that the NRL–SMO can perceptively detect the failure of the system sensor. Figures 23 and 24 are the tracking curve and error curve of the actual measured value and sliding mode estimated value of the system rotor current q-axis, respectively, and the same conclusion as the d-axis can be obtained from the figure.
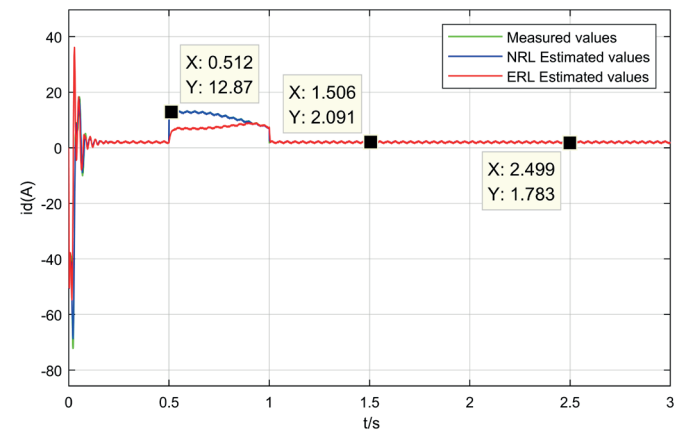

Fig. 21. Rotor current d-axis measurement and estimated value tracking curve

Bull. Pol. Acad. Sci. Tech. Sci. 69(3) 2021, e137389

11

R.Q. Li, W.X. Yu, J.N. Wang, Y. Lu, D. Jiang, G.L. Zhong, and Z.B. Zhou
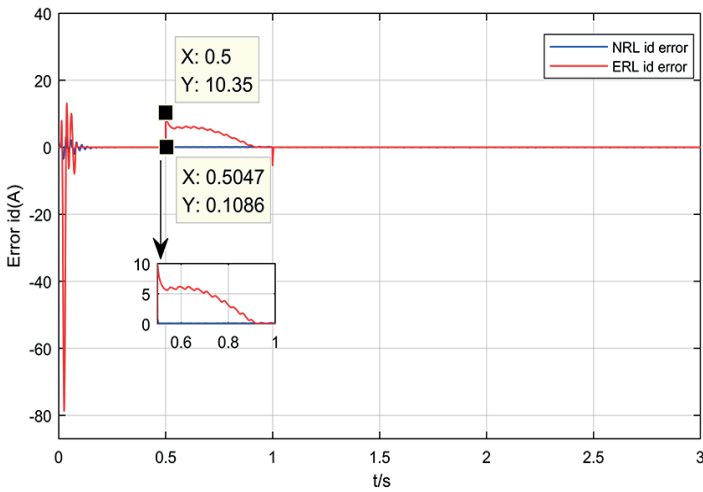

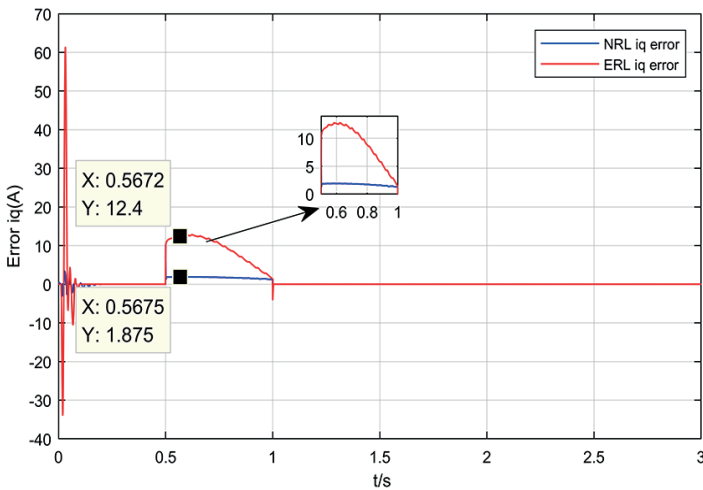Fig. 22. Error curve of rotor current d-axis measured value and estimated value

Fig. 24. Error curve of measured and estimated values of rotor current q-axis
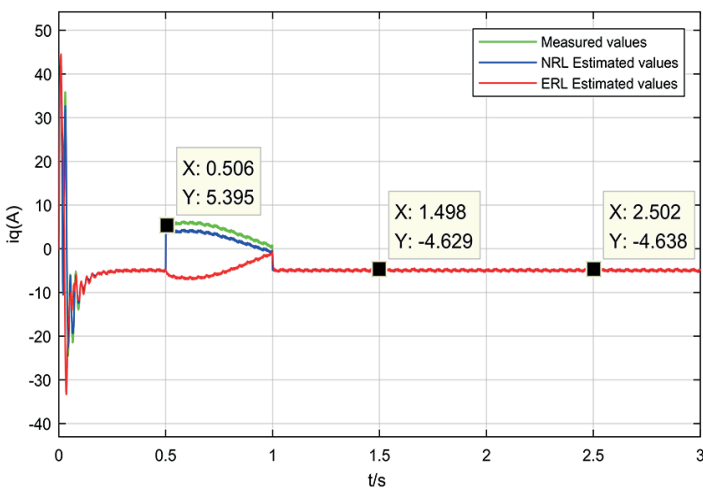

Fig. 23. Rotor current q-axis measured value and estimated valuetracking curve

Figures 25 and 26 are the change curves of the sliding mode control law based on the NRL and the ERL when the figure that after the sensor fails, the amplitude of the sliding mode control law based on the ERL changes from 1000 to about 2000 in the variable wind speed stage. The gain of the sliding mode control based on the NRL increases from 100 to 97980, and then quickly dropped to 1425. When the fault disappeared, and the system was completely stable, it dropped to 107. Compared with the sliding mode control law based on the NRL, the change of the sliding mode control law based on the ERL is not apparent, indicating that it is insensitive to the identification of system errors caused by sensor fault. When the rotor current sensor fails, the sliding mode control law based on the NRL has high amplitude, long duration, and fast change frequency. It verifies the idea that fault detection and diagnosis can be carried out through the sliding mode control law based on the NRL.
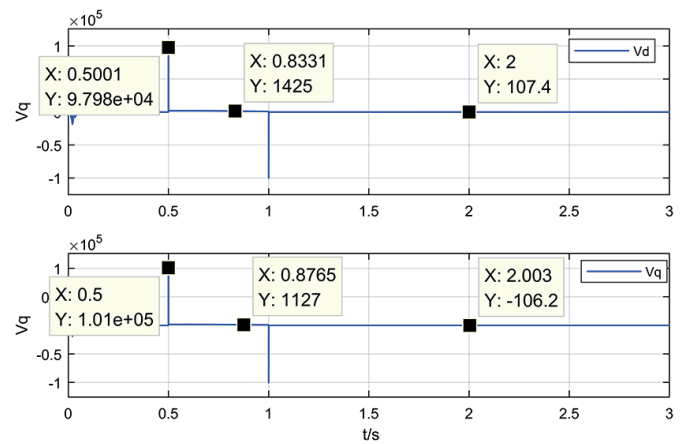

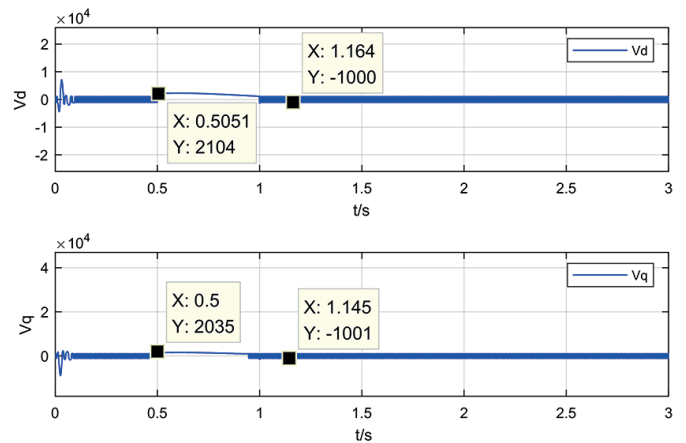Fig. 25. Variation curve of sliding mode control law based on the NRL

Fig. 26. Variation curve of sliding mode control law based on the ERL

Through the above experiments we can derive the performance differences between the two observer methods as shown in Table 2. This shows the effectiveness of the NRL-SMO proposed in this paper to track the system state and the fault detection.

12

Bull. Pol. Acad. Sci. Tech. Sci. 69(3) 2021, e137389

Table 2
Performance comparison between NRL-SMO and ERL-SMO

Method	System Performance			
	Respon-siveness	Tracking accuracy	Magnitude of chattering	Sensitivity to failure
NRL-SMO	Faster	About 0.005A	Very weak	Sensitive
ERL-SMO	General	About 0.01A	Stronger	Sensitive

6. Conclusion

In this paper, the sliding mode observer method is applied to the rotor current tracking and fault detection of DFIG. The main contribution of this paper is to introduce NRL method into the observer system to control chattering and anti-interference ability, which meets the requirement that the traditional sliding mode control method cannot meet the requirements of rapidity, smoothness and robustness at the same time. Then the sliding mode control law is used as the fault detection index of wind turbine system. The DFIG model experiments under different faults show that this method of NRL-SMO can realize the fault detection of DFIG and is better than the traditional observer method.

References

[1] Z. Hameed, Y.S. Hong, Y.M. Cho, S.H. Ahn, and C.K. Song. "Condition monitoring and fault detection of wind turbines and related algorithms: A review", *Renew. Sust. Energ. Rev.* 13(1), 1–39 (2009).

[2] A. Stefani, A. Yazidi, C. Rossi, F. Filippetti, D. Casadei, and G.A. Capolino, "Doubly fed induction machines diagnosis based on signature analysis of rotor modulating signals", *IEEE Trans. Ind. Appl.* 44(6), 1711–1721(2008).

[3] D. Shah, S. Nandi, and P. Neti, "Stator-interturn-fault detection of doubly fed induction generators using rotor-current and search-coil-voltage signature analysis", *IEEE Trans. Ind. Appl.* 45(5), 1831–1842 (2009).

[4] G. Stojčić, K. Pašanbegović, and T.M. Wolbank, "Detecting faults in doubly fed induction generator by rotor side transient current measurement", *IEEE Trans. Ind. App.* 50(5), 3494–3502 (2014).

[5] R. Roshanfekr and A. Jalilian, "Wavelet-based index to discriminate between minor inter-turn short-circuit and resistive asymmetrical faults in stator windings of doubly fed induction generators, a simulation study", *IET Gener. Transm. Distrib.* 10(2), 374–381 (2016).

[6] M.B. Abadi *et al.*, "Detection of stator and rotor faults in a DFIG based on the stator reactive power analysis", in *IECON 2014–40th Annual Conference of the IEEE Industrial Electronics Society* 2014 pp. 2037–2043.

[7] S. He, X. Shen, and Z. Jiang, "Detection and Location of Stator Winding Interturn Fault at Different Slots of DFIG", *IEEE Access* 7, 89342–89353 (2019).

[8] I. Erlich, C. Feltes, and F. Shewarega, "Enhanced voltage drop control by VSC–HVDC systems for improving wind farm fault ridethrough capability", *IEEE Trans. Power Deliv.* 29(1), 378–385 (2013).

[9] Ö. Göksu, R. Teodorescu, C.L. Bak, F. Iov, and P.C. Kjær, "Instability of wind turbine converters during current injection to low voltage grid faults and PLL frequency based stability solution", *IEEE Trans. Power Syst.* 29(4), 1683–1691 (2014).

[10] Z. Fan, G. Song, X. Kang, J. Tang, and X. Wang, "Three-phase fault direction identification method for outgoing transmission line of DFIG-based wind farms", *J. Mod. Power Syst.* 7(5), 1155–1164 (2019).

[11] L.G. Meegahapola, T. Littler, and D. Flynn, "Decoupled-DFIG fault ride-through strategy for enhanced stability performance during grid faults", *IEEE Trans. Sustain. Energy* 1(3), 152–162 (2010).

[12] F. Aguilera, P.M. De la Barrera, C.H. De Angelo, and D.E. Trejo, "Current-sensor fault detection and isolation for induction-motor drives using a geometric approach", *Control Eng. Pract.* 53, 35–46 (2016).

[13] S. Abdelmalek, S. Rezazi, and A.T. Azar, "Sensor faults detection and estimation for a DFIG equipped wind turbine", *Energy Procedia* 139, 3–9 (2017).

[14] M. Liu and P. Shi, "Sensor fault estimation and tolerant control for Itô stochastic systems with a descriptor sliding mode approach", *Automatica* 49(5), 1242–1250 (2013).

[15] Y.J. Kim, N. Jeon, and H. Lee, "Model based fault detection and isolation for driving motors of a ground vehicle", *Sens. Transducers* 199(4), 67 (2016).

[16] K. Xiahou, Y. Liu, L. Wang, M.S. Li, and Q.H. Wu, "Switching fault-tolerant control for DFIG-based wind turbines with rotor and stator current sensor faults", *IEEE Access* 7, 103390–103403 (2019).

[17] K.S. Xiahou, Y. Liu, M.S. Li, and Q.H. Wu, "Sensor fault-tolerant control of DFIG based wind energy conversion systems", *Int. J. Electr. Power Energy Syst.* 117, 105563 (2020).

[18] Z.Y. Xue, K.S. Xiahou, M.S. Li, T.Y. Ji, and Q.H. Wu, "Diagnosis of multiple open-circuit switch faults based on long short-term memory network for DFIG-based wind turbine systems", *IEEE J. Emerg. Sel. Top. Power Electron.* 8(3), 2600–2610 (2019).

[19] L. Jing, M. Zhao, P. Li, and X. Xu, "A convolutional neural network based feature learning and fault diagnosis method for the condition monitoring of gearbox", *Measurement* 111, 1–10 (2017).

[20] W. Teng, H. Cheng, X. Ding, Y. Liu, Z. Ma, and H. Mu, "DNN-based approach for fault detection in a direct drive wind turbine", *IET Renew. Power Gener.* 12(10), 1164–1171 (2018).

[21] M.N. Akram and S. Lotfifard, "Modeling and health monitoring of DC side of photovoltaic array", *IEEE Trans. Sustain. Energy* 6(4), 1245–1253 (2015).

[22] W. Gao and J.C. Hung, "Variable structure control of nonlinear systems, A new approach", *IEEE Trans. Ind. Electron.* 40(1), 45–55 (1993).

[23] C.J. Fallaha, M. Saad, H.Y. Kanaan, and K. Al-Haddad, "Sliding-mode robot control with exponential reaching law", *IEEE Trans. Ind. Electron.* 58(2), 600–610 (2010).

[24] Y. Liu, Z. Wang, L. Xiong, J. Wang, X. Jiang, G. Bai, R. Li, S. Liu, "DFIG wind turbine sliding mode control with exponential reaching law under variable wind speed", *Int. J. Electr. Power Energy Syst.* 96, 253–260 (2018).

[25] Z. Lan, L. Li, C. Deng, Y. Zhang, W. Yu, and P. Wong, "A novel stator current observer for fault tolerant control of stator current sensor in DFIG", in *2018 IEEE Energy Conversion Congress and Exposition (ECCE)*, 2018, pp. 790–797.

Bull. Pol. Acad. Sci. Tech. Sci. 69(3) 2021, e137389

13